3D Bioprinting Directly Onto Moving Human Anatomy

John J. O'Neill, Reed Johnson, Rodney L. Dockter, and Timothy M. Kowalewski Ph.D.

Abstract— **This paper establishes the feasibility of robotically 3D printing biomaterials such as alginate hydrogels onto moving human anatomy and a stationary plane. The alginate hydrogels used are *in-vivo* compatible and a proven biomaterial for tissue scaffolds. We developed a control scheme for precision material deposition via piezo microjetting while tracking in real-time to continuously sense anatomy location and deposits material in a predefined trajectory derived from two pre-selected target geometries. We show that multilayer 3D structures can be created on a moving human hand with 1.6 mm average error and 87.8 % overall accuracy.**

I. INTRODUCTION

Additive manufacturing has become a ubiquitous technology that allows for rapid prototyping, personalized design, and small-scale production. A variety of additive manufacturing methods exist, including fused-deposition modeling, selective laser sintering, and stereolithography. These methods utilize build materials such as plastics and metals. Materials are typically deposited onto a static, planar build surface and the object is built up layer by layer.

Recently, bioprinting technology has advanced in the field of tissue engineering via additive manufacturing techniques [1], [2]. Potential applications include tissue or organ regeneration, creation of biometric multi-layered skin tissue, and burn wound treatment [3]. One bioprinting approach has been to deposit living cells onto a surface using an inkjet system [4] noting several advantages over the more popular extrusion-based systems due to an inkjet's high-speed control and non-contact interface. In another approach, stem cells were embedded in a hydrogel solution and then deposited via pressure-driven nozzles onto skin wounds with the benefit of laser-based position sensing [5]. In this case the bioprinted stem cells provided better wound-closure rates than the manually applied gels. In [6] synthetic materials designed to mimic human skin were 3D-printed through pressure controlled channels on a linear 3-axis robotic stage. This study showed more accurate cell localization and 3D architecture of the reconstructed epidermis when compared with manual methods.

Prior art has demonstrated significant benefits of bioprinting for tissue engineering, however its scope has been constrained to depositing materials onto stationary targets. It traditionally emphasized planar substrates with open loop deposition trajectories [2]. In laboratory settings this has required printing onto phantom culture disks or printing onto sedated animal subjects. A case for printing directly onto anatomy has been made [5], [7]. In some clinical settings however, anatomy may be free-moving (such as the unfixtured hand of a burn patient that must move during therapy to maintain range of motion for skin grafts) or exhibit quasi-cyclic motion (such as a beating heart, breath-induced thorasic cavity motion, or vascular pulsatile throbbing of artery-proximate brain tissues). Therefore to increase the applicability of bioprinting, particularly in human-in-the-loop contexts, additive manufacturing techniques need to be augmented to allow for the deposition of material onto moving 3D surfaces. Previous attempts at tracking and drawing on a hand include either direct contact with the hand [8] or tracking the hand only in two degrees of freedom [9]. The gap in prior art has been the demonstration of an additive manufacturing technique capable of depositing 3D geometries of viable biomaterials directly onto unconstrained, non-planar, moving anatomy.

The objective of this paper is to demonstrate the feasibility of robotically depositing bioprinting-compatible materials directly onto unconstrained, moving human anatomy. Specifically, we demonstrate the 3D printing of alginate hydrogels onto (i) a non-stationary human hand (Figure 1) and (ii) a stationary plane to serve as a baseline. Alginate hydrogels are *in vivo*-compatible and a proven biomaterial for tissue scaffolds [10], [11]. A temporal coarse-fine approach controls precision material deposition via microjetting (a generalization of inkjetting to situations where the deposited material is not strictly an ink). Our system employs a real-time tracking algorithm to continuously sense anatomy location and deposit material onto it in a predefined trajectory derived from two pre-selected target geometries: a 2D block 'M' logo and a 3D stepped pyramid.
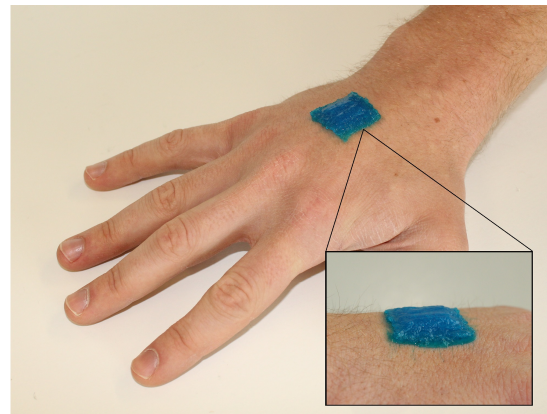

Fig. 1: Concept of 3D printing *in vivo* compatible biomaterials directly onto unconstrained, free-moving anatomy.

Department of Mechanical Engineering, University of Minnesota, 111 Church St SE, Minneapolis, Minnesota `oneil463@umn.edu`

II. METHODS

A. Hardware

Our custom additive manufacturing platform consisted of three primary components: a 3 DOF robotic platform, a material deposition system, and a sensing apparatus (Figures 2-3). The robotic platform used was an XYZ gantry system (Newmark Systems Inc, Rancho Santa Margarita, CA). This gantry stage has an XY travel distance of $600mm$ and a Z travel distance of $300mm$. Each dimension is actuated by a stepper motor, which is controlled with a DRV8825 stepper motor driver. The stepper motor drivers are in turn controlled by an ARM Cortex microcontroller (Teensy 3.2, PJRC Sherwood, OR).

Camera-in-hand velocity control was implemented with a proportional controller, where the velocity commanded to the steppers was proportional to distance error in X, Y, or Z measured between desired deposition location and actual measured location of the target. The gantry axes were aligned with the sensors to allow a one-to-one mapping. The proportional command was capped to between $2mm/s$ and $50mm/s$ to avoid unrealistic demands of the steppers as well as to keep the velocity from dropping near zero, as the drop-on-demand nature of the material deposition system is such that the robot does not need to stop at each point, but merely needs to glide over the point. The acceleration of the steppers was also capped to $312mm/s^2$ avoid undue stress on the system.
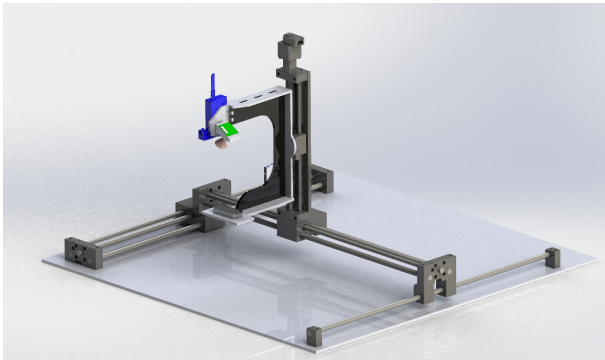

Fig. 2: Additive Manufacturing Gantry Setup

The material deposition system is an integral component of this design. While most 3D printers use extrusion, which deposits in a continuous bead, such an approach is not suitable for moving anatomy since the bead would need to be severed instantly if the anatomy moved out of position. For this approach we instead utilized an active deposition method based on a micro-jetting system capable of depositing micro-beads of solution. Specifically we utilized the PICO Pμlse jetting system (Nordson EFD, Westlake, OH). This system allows the deposition of viscous materials at a rate of $1kHz$ and orifice sizes of $50-600\mu m$. This selected range of orifice sizes roughly permits deposition of materials with viscosities between $200-500$ centipoises, though much larger ranges are available. The pulse timings used were $0.50ms$ pulse length and $8.00ms$ cycle length. With this approach we can employ
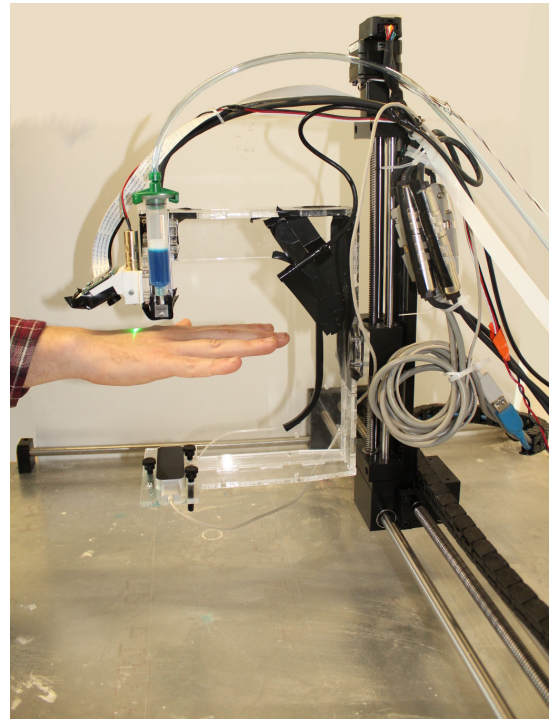

Fig. 3: Additive Manufacturing Deposition Onto a Moving Hand

a temporal-based manufacturing method wherein material is not deposited until the anatomy is positioned correctly beneath the extruder. Once material has been deposited, the flow is paused until correct positioning is achieved again.

The sensing modality consisted of two sub-components. For XY tracking we utilized an off-the-shelf hand tracking system (Leap Motion, San Francisco, CA). This system provides a 120 Hz framerate with a typical positioning accuracy near $1mm$ [12]. Unfortunately, the depth information from the Leap Motion is derived from stereo vision and is less accurate. The depth information is critically important for the deposition of subsequent layers to succeed and to minimize deposition errors from increased droplet travel distance. For accurate depth we designed a custom depth sensing system using a projected line green laser ($532nm$, $1mW$) and monocular camera (Figure 4).

The camera used was a hardware Raspberry Pi (Raspberry Pi Foundation, Cambridge, UK) camera that provides low-latency capture at $640x480$ resolution at $90Hz$. The laser produces a single horizontal line of green light in the camera frame. A custom support structure was designed to orient the optical axis of the camera at a $30°$ angle relative to the axis of the laser projection. This setup allows the laser line to be seen at a range of $10-60mm$. The green laser line appears in the image space as a vertical line. The location of the line G_j ($0-640$) is found in each row j of the image by finding the brightest pixel. Using the average G_j value of the line in the image, we can compute the distance in mm to the hand using a third-order polynomial, which accounts for radial distortion in the image. This analysis is performed on
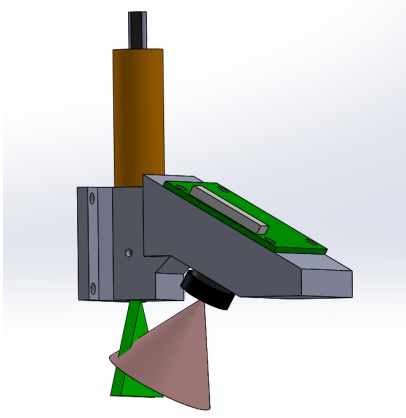
Fig. 4: Custom Laser Depth Sensor; Green Triangle Laser Field of Projection; Pink Cone Field of View of Camera

the Raspberry Pi using OpenCV running at approximately $2 - 4ms$ per frame.

Communication between sensors, actuators, and controllers is a key component of this system. Each sensor is responsible for communicating specific data to and from the central Teensy microcontroller. The microcontroller is in turn responsible for communicating commands to the various actuators.

B. Materials

Material selection was a critical design decision. While heated plastic filament hardens once deposited, viscous fluid biomaterials do not typically solidify quickly after deposition and therefore cannot maintain shape. Therefore a material solution was required that could be deposited through the jetting system (given the range of viscosities) and that could be cross-linked either automatically or via an added curing agent. Given these requirements, a sodium alginate solution ($(C_6H_8O_6)_n$) was chosen as the deposition material, with additives of detergent (sodium alkyl sulfates) as a surfactant to allow the solution to keep shape on the workspace prior to cross-linking, and colored food dye for the purpose of visualization and evaluation. Calcium chloride solution ($CaCl_2 \cdot 2H_2O$) was used as the cross-linking agent providing the calcium ions. As is further explained in [13], the free aqueous Ca^+ ions disperse into alginate and displace sodium to promptly cross-link it into a solid hydrogel.

The sodium alginate solution is produced by blending powdered sodium alginate with deionized water and then allowing the mixture to undergo degasification and set. The ratio of powder to water dictates the viscosity of the resulting solution. For the desired viscosity level of the sodium alginate, we used a ratio of $1g$ powder per $100ml$ water with $2ml$ of aqueous sodium alkyl sulfates and $0.1ml$ of blue food dye #1. For the calcium chloride spray, a ratio of $75g$ per $100ml$ water was used. After the deposition of a given layer of sodium alginate, the aqueous calcium chloride solution was manually applied to the entire build surface with an air brush to cross-link each layer.

The viscosity range of the jetting system and the viscosity of the sodium alginate solution serves well as a surrogate for the eventual bioprinting of cells or other non-alginate bio-inks commonly used in extrusion as in [1], [2].

C. Software

For the tracking, control and logic of the additive manufacturing process, we utilized a custom software stack implemented on a desktop PC running Ubuntu and the Robot Operating System (ROS) [14]. The complete stack consisted of 5 primary components as outlined in Algorithm 1, where V_{motor} is a stepper velocity command and C_{jet} is a logic signal to the jetting system.

Algorithm 1: Deposition Control Algorithm

---

1   **MovingDeposition** $(I_{template})$
     inputs: A template of x, y locations $I_{template}$
2   **foreach** *coordinate* $S_i \in I_{template}$ **do**
3   **while** *true* **do**
4              $P_t(x, y) \leftarrow currentLeap(x, y)$;
5              $P_t(z) \leftarrow currentLaserDepth(z)$;
6              $D_t \leftarrow S_i$;
7              $E_t \leftarrow P_t - D_t$;
8   **if** $|E_t| < threshold$ **then**
9                  $V_{motor} \leftarrow (P_t - D_t)K_p$;
10                  $C_{jet} \leftarrow 0$;
11   **else**
12                  $V_{motor} \leftarrow V_{min}$;
13                  $C_{jet} \leftarrow 1$;
14   *break*;
15   **end**
16   **end**
17   **end**
18      $V_{motor} \leftarrow (0, 0, 0)$;
19      $C_{jet} \leftarrow 0$;

The first step in this method is to continuously track the position of the anatomy ($P_t = [x, y, z]$) relative to the extrusion head. For this position x and y are sensed via the Leap motion, and z is sensed with the laser distance sensor.

Given the known instantaneous position of the anatomy, we then query a predefined template for the state of that location ($S_i = [x, y, z]$). This template is stored as a series of 2-dimensional binary image matrices with x, y determined by an individual frame and z determined by the frame index. If the corresponding pixel requires material, a low latency command is sent to the jetting system and the corresponding pixel is marked as complete (Figure 5). This process is continued until all pixels for the current frame have been completed, and then the next frame is queried.

Determining the optimal trajectory to take for deposition of a single layer requires comparing the end effector's current velocity with the vector to all remaining deposition pixels in the current layer. The end effector's velocity in z is controlled by the laser height sensor through a proportional controller. In x and y the velocity vector is taken as the difference
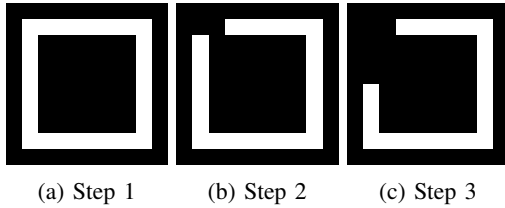
| (a) Step 1 | (b) Step 2 | (c) Step 3 |

Fig. 5: Deposition Remaining for a Single Frame

$\Delta P = P_t(x,y) - P_{t-1}(x,y)$ while the vector to remaining pixel i is taken as $V_i = D_i(x,y) - P_t(x,y)$. The difference in bearing between these two headings is computed in Equation 1, where α is confined to the interval $[0,2]$.

$$\alpha = 1 - \Delta P \cdot V_i \qquad (1)$$

We compute the scaled distance to all remaining deposition pixels as in Equation 2, where N_{px} is the width of the binary template matrix so that β is also confined to the interval $[0,2]$.

$$\beta = 2|V_i|/N_{px} \qquad (2)$$

All potential targets are evaluated and the target with the lowest cost γ as defined in Equation 3 is chosen as D_t.

$$\gamma = \alpha + \beta \qquad (3)$$

Given the instantaneous desired deposition location (D_t) and the instantaneous anatomy location (P_t) we can compute the end-effector error $E = P_t - D_t$. From this error we compute the required end-effector velocity $V = E * K_p$ where K_p is a gain parameter.

D. Experimental Design

To evaluate the accuracy and reliability of the proposed system for 3D printing a hydrogel directly onto moving human anatomy, we performed four experiments of increasing complexity.
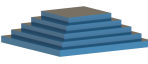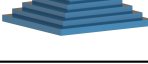
The first experiment was designed to examine the baseline accuracy of the gantry system and hydrogel material for 2D deposition in a known pattern on a stationary surface. For this experiment a block 'M' pattern (Table I) was deposited on a stationary build plate in a $100x100mm$ area. The deposition pattern was followed in an open loop fashion without tracking of the target substrate position, only encoder feedback of the stepper joints. To provide sufficient material for a complete layer, the pattern was printed three times, spraying the aqueous calcium chloride solution to cross-link between each run.

The second experiment was designed to assess the accuracy of the deposition system in 2D for moving anatomy. For this experiment a hand was placed below the deposition jet and allowed to move freely. Again the block 'M' pattern (Table I) was deposited on the hand while the hand was continuously tracked via the sensing system. Again the pattern was printed three times, spraying the aqueous calcium chloride solution to cross-link between each run.

The third experiment was designed to assess the accuracy of this system with regards to multiple layers. For this experiment, multiple layers of a pyramid template were deposited on a stationary build plate. The pyramid was made up of 5 stacked squares, each smaller than the prior step, creating the pyramid template in Table I. Again the pattern was printed three times per layer, spraying the aqueous calcium chloride solution to cross-link between each run.

The fourth experiment was designed to the assess the accuracy of this system with regards to a multi-layer model on a moving hand. For this experiment an unconstrained hand was again placed below the deposition jet. This setup utilized the pyramid model (Table I) from Experiment 3. Each layer was deposited sequentially onto the moving hand and the pattern was printed three times per layer, spraying the aqueous calcium chloride solution to cross-link between each run.

TABLE I: Experiment Summary

Experiment	Substrate	Target Object Geometry	Total Layers
1	Stationary		3
2	Unconstrained		3
3	Stationary		15
4	Unconstrained		15

E. Experimental Evaluation

The deposition pattern was scanned in 2D for Experiments 1 and 2 with a color flatbed scanner at $600dpi$ so that the $100x100mm$ deposition area became an image with dimensions $2362x2362px$. In 3D for Experiments 3 and 4 the deposition pattern was scanned with a 3D scanning system (Artec Spider, Artec 3D, Luxemburg) with a resolution of $G_s = 0.04mm$. The scanned point cloud of the surface was converted to voxels at $600dpi$ to match Experiments 1 and 2. The scans were then programmatically registered with the template via a rigid transformation to minimize error.

Error was calculated at each pixel or voxel in the template as the deviation in value between the template image and the corresponding pixel in the scanned image. True Positive (TP) locations were those where deposition occurred in the desired location (correct deposit). False Negative (FN) locations were those where deposition was desired but did not occur (missing deposit). False Positive (FP) locations were those where deposition occurred but was not desired (incorrect deposit). The TP and FN values were used to compute both the True Positive Rate (TPR) and False Negative Rate (FNR) (Equations 4 and 5 respectively) where the total number of desired pixels or voxels (N_t) was used as the total Condition Positive. The FP value was used to compute the False Discovery Rate (FDR) (Equation 6), where the number of deposited pixels or voxels (N_s) was used as the total Test Outcome Positive. The average error between the

outer surface of the template and the surface of the scan was also used as a performance metric to give an outer-shell accuracy in mm.

$$TPR = \frac{\sum(I_{template} \cap I_{scan})}{\sum(I_{template})} \quad (4)$$

$$FNR = \frac{\sum(I_{template} \cap \neg I_{scan})}{\sum(I_{template})} \quad (5)$$

$$FDR = \frac{\sum(\neg I_{template} \cap I_{scan})}{\sum(I_{scan})} \quad (6)$$

Registration between the 3D scan of the resultant deposition and the 3D template was achieved via an Iterative Closest Point (ICP) correspondence. Error was calculated as the deviation between each point in the 3D scan and the corresponding point in the 3D template (Equation 7). The TP, FN, and FP measures were computed in 3D between the scanned structure and the pyramid model scaled to the height of the scan. Given a discrete x, y location in the 3D scan, TP locations were those where the z height was the same as the model, FN locations were those where too little material was deposited, and FP locations were those where too much material was deposited. These values were then used to compute the TPR, FNR, and FDR rates (similar to Equations 4-6). For each x, y scan location, the z height of the scan was compared with the corresponding z height in the model. The height difference was multiplied by G_s which represents the voxel size dictated by the 3D scan resolution. In this case $G_s = 0.04mm$. This provides a volumetric representation of the difference between desired geometry and scan. The mean layer height for the complete structure was calculated as the total height divided by the number of layers.

$$E = \sum_{x=1}^{m} \sum_{y=1}^{n} (Z_{template}(x,y) - Z_{scan}(x,y))G_s^2 \quad (7)$$

III. RESULTS

A. Experiment 1: 2D Stationary Deposition

The baseline printing accuracy for the proposed gantry and deposition system was assessed by depositing the template from Table I onto a stationary build plate (Figure 6). The resultant deposition, threshold image, and comparison is given in Figure 7. The accuracy and other metrics are given in Table II.
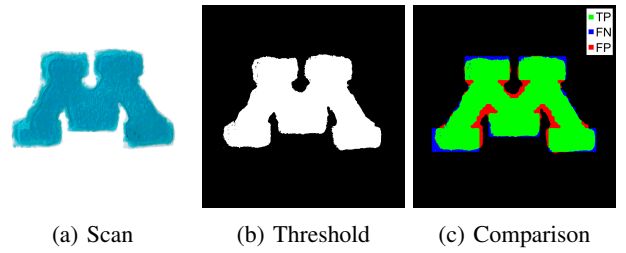

Fig. 6: 2D Deposition Resultant

(a) Scan	(b) Threshold	(c) Comparison

Fig. 7: Exp. 1, 2D Stationary Deposition Comparison

TABLE II: Experimental Results

Experiment	TPR (%)	FNR (%)	FDR (%)	Mean Error (mm)	Time (min)
1: 2D Stationary	94.9	5.1	10.8	0.50	11.0
2: 2D Unconstrained	92.6	7.3	17.7	0.73	16.1
3: 3D Stationary	91.5	8.5	38.2	0.95	37.3
4: 3D Unconstrained	87.8	12.3	36.1	1.60	40.9

* TPR: True Positive Rate (correct deposit), FNR: False Negative Rate (missing deposit), FDR: False Discovery Rate (incorrect deposit)

B. Experiment 2: 2D Unconstrained

The second experiment was designed to assess the accuracy with which the proposed system could deposit the template image on an unconstrained hand. The hand moved at an average velocity of $5mm/s$ up to a maximum of $25mm/s$. We again utilized the template image from Table I. The resultant deposition, threshold image, and comparison is given in Figure 8. The accuracy and other metrics are given in Table II.

C. Experiment 3: 3D Stationary

The third experiment was designed to assess the accuracy of the proposed system while depositing a multiple-layer model on a stationary build plate utilizing the pyramid template from Table I. The resultant scan of the deposition is given in Fig 9a. An error map indicating the regions where incorrect deposition occurred is given in Figure 9b. The average deposition layer height for this template was $0.79mm$. The accuracy and other metrics are given in Table II.

D. Experiment 4: 3D Unconstrained

The fourth experiment, 3D Dynamic, was designed to assess the accuracy with which the proposed system could deposit a multi-layer template onto an unconstrained hand
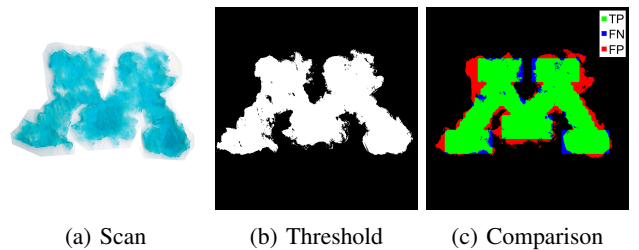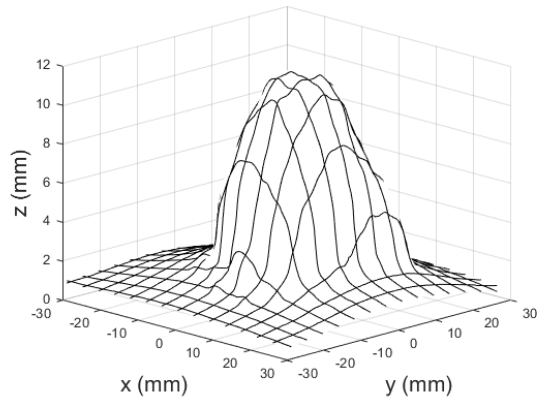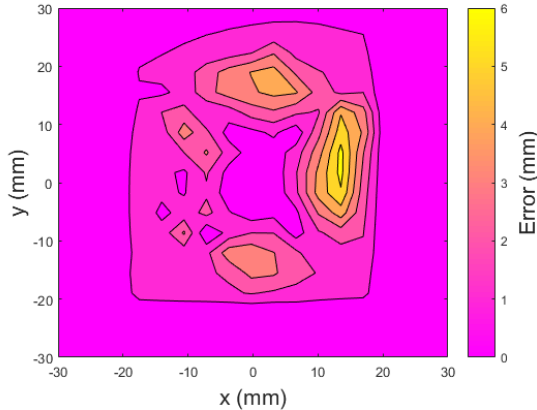

(a) Scan	(b) Threshold	(c) Comparison

Fig. 8: Exp. 2, 2D Unconstrained Comparison

(a) 3D Scan
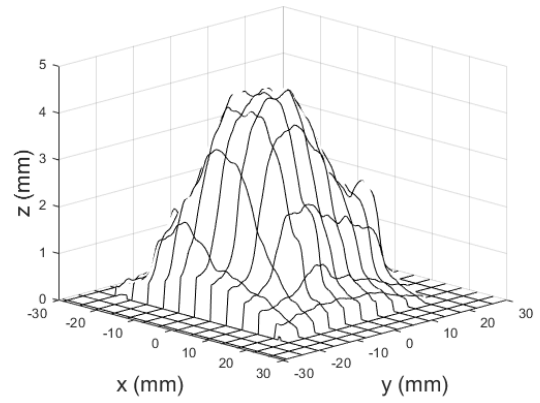

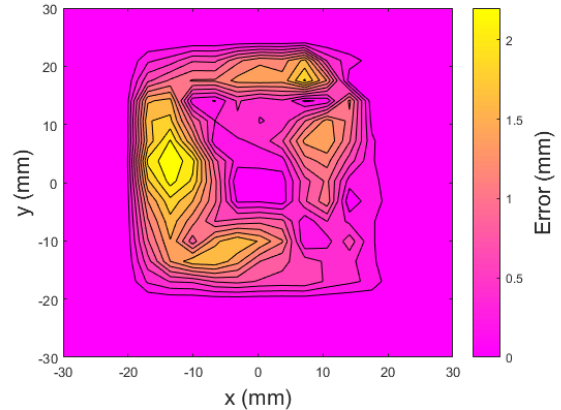(a) 3D Scan

(b) Error Map

(b) Error Map

Fig. 9: Exp. 3, 3D Stationary Comparison

Fig. 10: Exp. 4, 3D Unconstrained Comparison

moving similarly to Experiment 1. We utilized the sequence of template images for the pyramid model (Table I). The 3D scan and comparison is given in Figure 10. The accuracy and other metrics are given in Table II.

IV. DISCUSSION

We presented a system for successfully bioprinting desired alginate hydrogel geometries onto unfixtured, moving substrates. To our knowledge this is the first successful attempt at 3D printing onto moving human anatomy. Our system uses precise piezo-electric jetting deposition of viscous hydrogels that allows decoupling of deposton control timing from motion planning and robotic actuation. For a baseline control case, the system achieved an average error of 0.50 mm with 94.9% overall deposition accuracy in a 2D analysis of a planar stationary task (Experiment 1). When the same geometry was printed on an unconstrained hand (Experiment 2), average positional error increased by 0.33 mm (46%) and overall accuracy dropped only slightly by 2.5%. This is a favorable result particularly in light of the unconstrained, natural motion of the hand. Print times were comparable to typical 3D printing speeds for these volumes and did not increase dramatically with the introduction of motion. The change from 2D to 3D stationary cases (adding 15 layers

in Experiment 3 compared with just 3 layers in Experiment 1) saw significantly larger increases in error compared to changing from 2D stationary (Experiment 1) to 2D dynamic cases (Experiment 2). This underscores some of the accuracy limitations of the selected material deposition and cross-linking processes, independent of substrate motion. Notably, the deposited alginate solution remains fluid and has ample time to flow away before calcium chloride solution is applied and Ca^+ ions diffuse through the fluid to displace sodium and cross-link the gel into a solid. This is observable in the bunching "roll off" of material indicated by lighter regions in Figures 9b and 10b and visible as non-flat sides in Figures 6 and 1.

In this approach we have used a proven bioprinting-compatible alginate hydrogel solution which has viscosities orders of magnitude higher than traditional low viscosity (≈ 1 centipoises) aqueous inkjets. Our jetting hardware can easily scale to a wide viscosity range yet maintain cell viability as evident in [15]. In principle, this implies that our system is immediately compatible with a wide range of existing bio-inks in widespread use and commonly available to bioprinting research, not just hydrogels (e.g. vendors like biobots). This includes photo-curable or temperature curable

inks with simple modifications in our hardware.

There are several limitations in this work. We did not print viable bio-inks and confirm cell survival, though it is well established in the literature with jetting. We do not implement closed-loop sensing and deposition of the material geometry. This is in principle quite feasible with our laser distance sensing and will be explored in future work. However, despite the delays in cross linking, the resulting errors are not substantial. Our deposition of aqueous calcium chloride via manual airbrush is a source of error, delay, and variation between experiments. It would be simple to automate this procedure with an additional jetting head (such as in [10]), but we plan to pursue photocurable materials in the future due to the quicker response time. The desired geometries we printed were unrealistic for medical applications. While they demonstrated programmability of desired geometries, we did not include straight walls or overhanging features— items particularly difficult to 3D print with fluids without, for example, changing orientation relative to gravity. Future work will include adapting our sensing technology to track more varied human anatomy including localized stretch, allowing this system to deposit material onto tissues and organs. We intend to coordinate with researchers from tissue engineering groups to utilize viable bio-inks within our system and explore its accuracy for more complex, realistic geometries.

V. CONCLUSION

This work has demonstrated the feasibility of robotically depositing bioprinting-compatible materials directly onto unconstrained, moving human anatomy with submillimeter average error rates for 2D surfaces and millimeter-range average error rates for 3D geometries.

ACKNOWLEDGMENT

REFERENCES

[1] S. V. Murphy and A. Atala, "3D Bioprinting of Tissues and Organs," *Nature biotechnology*, vol. 32, no. 8, pp. 773–785, 2014.

[2] I. T. Ozbolat and Y. Yu, "Bioprinting toward organ fabrication: challenges and future trends," *IEEE Transactions on Biomedical Engineering*, vol. 60, no. 3, pp. 691–699, 2013.

[3] Y.-J. Seol, H.-W. Kang, S. J. Lee, A. Atala, and J. J. Yoo, "Bioprinting technology and its applications," *European Journal of Cardio-Thoracic Surgery*, p. 148, 2014.

[4] M. Nakamura, A. Kobayashi, F. Takagi, A. Watanabe, Y. Hiruma, K. Ohuchi, Y. Iwasaki, M. Horie, I. Morita, and S. Takatani, "Biocompatible inkjet printing technique for designed seeding of individual living cells," *Tissue engineering*, vol. 11, no. 11-12, pp. 1658–1666, 2005.

[5] A. Skardal, D. Mack, E. Kapetanovic, A. Atala, J. D. Jackson, J. Yoo, and S. Soker, "Bioprinted amniotic fluid-derived stem cells accelerate healing of large skin wounds," *Stem cells translational medicine*, vol. 1, no. 11, pp. 792–802, 2012.

[6] V. Lee, G. Singh, J. P. Trasatti, C. Bjornsson, X. Xu, T. N. Tran, S.-S. Yoo, G. Dai, and P. Karande, "Design and fabrication of human skin by three-dimensional bioprinting," *Tissue Engineering Part C: Methods*, vol. 20, no. 6, pp. 473–484, 2013.

[7] X. Cui, T. Boland, D. D D'Lima, and M. K Lotz, "Thermal inkjet printing in tissue engineering and regenerative medicine," *Recent patents on drug delivery & formulation*, vol. 6, no. 2, pp. 149–155, 2012.

[8] J. J. O'Neill and T. M. Kowalewski, "Online free anatomy registration via noncontact skeletal tracking for collaborative human/robot interaction in surgical robotics," *Journal of Medical Devices*, vol. 8, no. 3, p. 030952, 2014.

[9] A. French, J. O'Neill, and T. M. Kowalewski, "Design of a dynamic additive manufacturing system for use on free-moving human anatomy," *Journal of Medical Devices*, vol. 10, no. 2, p. 020941, 2016.

[10] T. Xu, C. Baicu, M. Aho, M. Zile, and T. Boland, "Fabrication and characterization of bio-engineered cardiac pseudo tissues," *Biofabrication*, vol. 1, no. 3, p. 035001, 2009.

[11] T. Andersen, P. Auk-Emblem, and M. Dornish, "3d cell culture in alginate hydrogels," *Microarrays*, vol. 4, no. 2, pp. 133–161, 2015.

[12] F. Weichert, D. Bachmann, B. Rudak, and D. Fisseler, "Analysis of the accuracy and robustness of the leap motion controller," *Sensors*, vol. 13, pp. 6380–6393, 2013.

[13] K. Y. Lee and D. J. Mooney, "Alginate: properties and biomedical applications," *Progress in polymer science*, vol. 37, no. 1, pp. 106–126, 2012.

[14] M. Quigley, K. Conley, B. Gerkey, J. Faust, T. Foote, J. Leibs, R. Wheeler, and A. Y. Ng, "Ros: an open-source robot operating system," in *ICRA workshop on open source software*, vol. 3, no. 3.2. Kobe, Japan, 2009, p. 5.

[15] S. Di Risio and N. Yan, "Piezoelectric ink-jet printing of horseradish peroxidase: effect of ink viscosity modifiers on activity," *Macromolecular Rapid Communications*, vol. 28, no. 18-19, pp. 1934–1940, 2007.